



## Adaptive notch-filtration to effectively recover photoplethysmographic signals during physical activity



Xiaoyu Zheng<sup>a</sup>, Vincent M. Dwyer<sup>a</sup>, Laura A. Barrett<sup>b</sup>, Mahsa Derakhshani<sup>a</sup>, Sijung Hu<sup>a,\*</sup>

<sup>a</sup> Wolfson School of Mechanical, Electrical, and Manufacturing Engineering, Loughborough University, Loughborough LE11 3TU, UK

<sup>b</sup> School of Sport, Exercise and Health Sciences, Loughborough University, Loughborough LE11 3TU, UK

### ARTICLE INFO

#### Keywords:

Motion artefacts (MA)  
Multi-wavelength illumination optoelectronic patch sensor (mOEPS)  
Adaptive notch-filtration (ANF)  
Real-time signal processing  
Heart rate (HR)  
Respiration rate (RR)

### ABSTRACT

Physical activity can severely influence the quality of photoplethysmographic (PPG) signals due to motion artefacts (MA). This study aims to extract heart rate (HR) and respiration rate (RR) values from raw PPG signals captured from a multi-wavelength illumination optoelectronic patch sensor (mOEPS) during physical activity of different intensities, and to do this in an effective manner. The proposed method, combined with a 3-axis accelerometer as a motion reference, was developed for the extraction of the desired PPG signals. The adaptive notch-filtration architecture (ANFA) comprises three parts: 1) the adaptive moving average filter, 2) the adaptive notch filter, and 3) extraction for physiological parameters. 24 healthy subjects completed four stages of exercise of increasing intensity. The recovered PPG signals for the calculation of HR and RR were comparable to the measurements from commercial devices, with an average absolute error for HR of < 1.0 beats/min for the IEEE-SPC dataset, and 1.3 beats/min for HR, and 2.8 breaths/min for RR, from the in-house dataset. The ANFA has been proofed to have a good robustness and low complexity to be suitable for application in real-time physiological monitoring.

### 1. Introduction

Photoplethysmography (PPG) is a low-cost, non-invasive, optical technique that can be used to measure vital physiological signs, such as heart rate (HR), heart rate variability, oxygen saturation, and respiration rate (RR) [1]. As a consequence PPG-based health monitoring has been widely adopted for use in wearable devices [2,3]. The periodic variations in the PPG signal, related to the cardiac rhythm and breathing changes, make it possible to determine HR and RR [4,5]. Despite the wealth of physiological information that the PPG signal can provide, it is easily disturbed by artefact noise generated from a variety of noise sources, such as the modification of the optical properties of the internal tissues due to for example tissue compression, poor blood perfusion, motion artefact (MA), the distance between the optical sensor and skin surface, and electromagnetic and electronic noise [6,7].

Accurate HR and RR values are acquired from PPG signals affected by noise artifacts using a number of different methods including: independent component analysis (ICA) [8], frequency-domain ICA [9], empirical mode decomposition (EMD) [10], improved complete ensemble empirical mode decomposition with adaptive noise (ICE-EMDAN) [11], a wavelet-transform method [12] and Kalman filtering

[13]. However, these methods are generally only suitable for use during relatively low-intensity physical activity/movement [14]. The relationship between acceleration and the PPG signals has also been exploited to extract PPG signals in the case of low levels of MA [15] and the use of acceleration data has become a versatile aid for the removal of MA. An adaptive noise cancellation method using recursive least squares (RLS) [16] and an adaptive-size least mean squares (AS-LMS) adaptive filter [17] have been applied to weaken the noise artefacts with the aid of acceleration measurements, as they are associated with the intensity of motion. These adaptive filtering (AF) methods perform better during low-intensity than high-intensity physical activity [18]. The performance of AF is highly influenced by the quality of the reference signal, i.e. the acceleration signal as the acceleration signal is linearly related to the MA. Such AF is not easily applied to real-time MA cancellation [19].

To overcome these shortcomings, Zheng et al. [20] proposed an effective method (TROIKA) to remove MA from wrist-worn PPG which has improved noise removal ability and robustness. However in order to provide accurate HR values the TROIKA method is dependent on there being sparse signal decomposition. The performance of TROIKA can be improved by joint sparse spectrum reconstruction (JOSS) [21] which exploits the fact that the PPG and 3-axis acceleration spectra have

\* Corresponding author.

E-mail address: [S.Hu@lboro.ac.uk](mailto:S.Hu@lboro.ac.uk) (S. Hu).

common features to generate a spectral estimation of these signals using a JOSS model. Although the JOSS method can effectively remove in-band MAs during low and high-intensity physical activity, it cannot be used during real-time monitoring due to its high computational complexity. A time-varying spectral filtering algorithm has been recently developed in [22], which compares the frequency of the PPG spectrum with the acceleration spectra. The frequency peaks generated by MA can be distinguished from the PPG spectrum. Due to the demand of larger data processing capacity for sample-by-sample windowing process, it is difficult to deploy the algorithm into a wearable electronic system for the real-time recovery of PPG signals. Recently, Islam et al. [23] introduced a modified spectral subtraction scheme with a composite motion artifact reference (SPECMAR) method along with a synthetic MA reference. Again, a fusion method was reported in [1], using band-stop filters to remove the in-band MA. The method then applies a band-stop filter with a rejection frequency related to the acceleration spectrum under static conditions, which can be easily achieved on a primary processor platform.

Referring to these methods, the purpose of this study was to explore how to effectively recover a PPG signal against MA corruption in order to extract physiological parameters in real-time. To achieve this, an adaptive notch-filtration architecture (ANFA) was proposed as a practicable signal processing platform and developed for reduction of MA in different physical activity intensities in order to recover cleansed PPG signals. The ANFA is intended for real-time use and the filtration algorithm has low complexity, but still allows the user to obtain accurate physiological readings. The study includes the following aspects:

- (1) The proposed ANFA to be effectively applied for the in-band and out-of-band MA at different exercise intensities, to obtain MA-free PPG signals.
- (2) More accurate HR and RR readings to be determined from the recovered PPG signals by the means of the ANFA.
- (3) Lower absolute error values to be delivered by the ANFA along with a 24 subject engaged protocol at different physical activity intensities.
- (4) The deployment of the ANFA into a wearable electronic system to be durable to achieve real-time health monitoring.

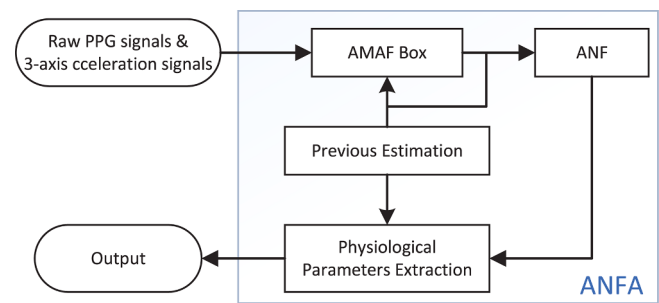


**Fig. 1.** Adaptive notch-filtration architecture (ANFA) comprising of 1) AMAF Box, 2) ANF, and 3) Extraction for physiological parameters.

### 2.1. Adaptive Moving Average Filter (AMAF) Box

Prior to the procedure of ANFA, 3-axis acceleration signals are selected through a 8<sup>th</sup> order IIR Butterworth bandpass filter which has a passband of 0.2 Hz to 6 Hz. These signals are then subjected to Fast Fourier Transform (FFT). The raw PPG signals obtained from green illumination of the mOEPS are usually first filtered to remove any slowly varying background using an adaptive moving average filter (AMAF). To obtain better PPG signals, the fitting parameter is automatically adapted to the current HR during the measurement period for various sliding windows. The input signal sequence is  $S_{in} = [s_1, s_2, s_3, \dots, s_n]$  and the fitting parameter is  $p$ . The input raw data sequence is improved by a simple background subtraction, where the background is estimated using a  $p$ -point moving average filter. The output  $S_{out}(n)$  at the current point  $n$  is represented by the difference between the signal value there, and the mean of values at the  $(n - p/2)^{th}$  to  $(n + p/2 - 1)^{th}$  points as below:

$$S_{out}(n) = \frac{1}{p} \sum_{k=n-p/2}^{n+p/2-1} (S_{in}(n) - S_{in}(k)). \quad (1)$$

It is informative to see the effect of this filter in the frequency domain. For an arbitrary frequency component,  $S_{in}(n) = \exp(2\pi jfn/F_s)$ , in the measured raw data, the output obtained from this process of background removal  $S_{out}$  is

$$\begin{aligned} S_{out}(n) &= \exp(2\pi jfn/F_s) \left( 1 - \frac{\exp(2\pi jfp/2F_s) + \dots + 1 + \dots + \exp(-2\pi jf(p/2-1)/F_s)}{p} \right) \\ &\approx \exp(2\pi jfn/F_s) (1 - \text{sinc}(pf/F_s)) \\ &= H_{AMAF}(f; p) \exp(2\pi jfn/F_s). \end{aligned} \quad (2)$$

## 2. Methods and Materials

The block diagram of the proposed ANFA is depicted in Fig. 1. The proposed method consists of three essential parts: 1) adaptive moving average filter (AMAF) box, 2) adaptive notch filter (ANF), and 3) extraction for physiological parameters. Firstly, a background removal process is performed on the raw PPG signals, adopting an AMAF and a bandpass filter for the purpose of removing the out-of-band noise caused by a poorly attached sensor, external electromagnetic impact or low blood perfusion. Secondly, the adaptive notch filter is employed to remove in-band MA from the filtered PPG signals, with the aid of the 3-axis acceleration signals, by finding a set of peaks from the frequency spectrum of the cleaned signals. Finally, the algorithm to extract physiological parameters (here HR and RR) from the recovered PPG signals was designed to ensure improved accuracy compared with previous work. In the following sections, the ANFA is presented in detail.

The sinc function has a broad lobe, centred around  $f = 0$  and of peak height unity, and a number of smaller side lobes. After subtraction  $H_{AMAF}(f; p)$  removes this broad lobe and thus represents an adaptive high-pass filter, with an adaptation parameter  $p$  which alters the high-pass cut-off frequency to  $f \approx F_s/p \approx 256/p$  Hz (at the current sample rate of  $F_s = 256$  Hz). Consequently choosing  $p = 256$  samples ensures all  $HR > 60$  beats/min will not be cut off. Similarly,  $p$  might be reduced to  $\approx 64$ , or a cutoff of 15 breaths/min, when extracting RR.

With the time variation of HR or RR, the bandwidth of the AMAF window must adjust (under adaptation) to reflect the change. The adaptation rule is set to keep the value  $H_{AMAF}(f_{HR/RR})$  roughly fixed, i.e.,  $pf_{HR/RR}/F_s \approx 1$ . This is implemented, for the  $m^{\text{th}}$  interval, by using the frequency of previous HR or RR as

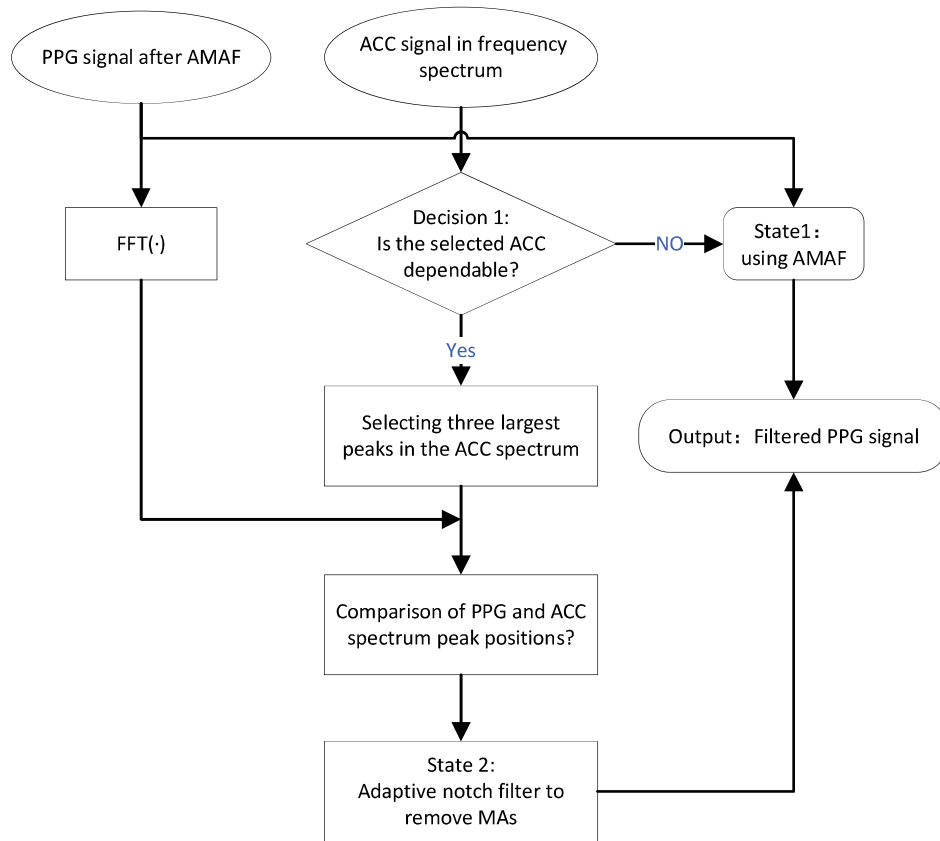


**Fig. 2.** The flowchart of the adaptive notch filter.

$$\frac{p(m) \times f_{HR/RR}(m-1)}{F_s} = 1. \quad (3)$$

where all frequencies are in Hz. In this way  $p = 256$  is used in the case that  $f_{HR} = 1$  Hz. After the above procedure, an 8<sup>th</sup> order digital Butterworth IIR band-pass filter acts on the  $S_{out}$  to remove the impact of out-band noise with the same cut-off frequencies of 0.2 to 6 Hz as used earlier for acceleration signals.

## 2.2. Adaptive Notch Filter for In-band Motion Artefacts Removal

To further remove MA, the pre-processed PPG signal, along with 3-axis acceleration references, are loaded into the signal processing system, here denoted as ANF and shown in Fig. 2. Suitable notch filters are selected in each sliding time window rather than using a fixed notch filter, as in [1].

Prior to processing with the ANF, the acceleration signal (ACC) is chosen as a reference noise signal in each sliding time window. Precisely, to minimize the complexity of ANF, the analysis of only one axis (i.e.,  $x$ -axis) of the acceleration signal was considered [1]. Next, it needs to be verified whether the peaks in the ACC spectrum are related to MA. Such peaks are expected to present as fairly large during strenuous exercise. When the 3-axis acceleration spectrum is too broad, the useful MA component cannot easily be extracted by exploring the acceleration signal. Thus, Decision 1 is adopted to check the largest spectral peak in the selected acceleration data as shown in Fig. 2. When the largest spectral peak is less than some threshold ( $th_1$ ), it indicates that the current motion peak does not feed through to the PPG signal significantly and the MA interference is relatively trivial.

An appropriate value for threshold  $th_1$ , which separates exercise and rest, will also depend upon the length of the FFT, i.e.,  $N_{FFT}$ . For the value used here ( $N_{FFT} = 8192$ ), including zero-padding, a value of  $th_1 = 50$  was found to be appropriate. For other values of  $N_{FFT}$ , one should

include a factor of  $N_{FFT}/8192$  in  $th_1$ . For  $N_{FFT} = 1024$ , necessary for a near-real-time situation,  $th_1$  would need to be adjusted to around  $50/4 = 12.5$  for the same effect. In the case that the peak is below threshold, the AMAF filtered PPG signal is used as the algorithm output (State 1). Thus, the ACC signal is unnecessary in this particular sliding time window, and State 2 is triggered as detailed below.

A 2<sup>nd</sup> infinite impulse response (IIR) filter can be used to implement the notch filter in State 2, which is always stable and has a linear delay [24]. The general form of the transfer function [25] in this case is:

$$H(z) = \frac{r^2 - (1+r^2)\cos(\omega)z^{-1} + z^{-2}}{1 - (1+r^2)\cos(\omega) + r^2z^{-2}}, \quad (4)$$

where

$$\omega = \frac{2f_c}{f_s}, r = \frac{f_c}{\mu}. \quad (5)$$

In (4) and (5),  $r$  controls the bandwidth of the notch filter and  $\mu$  is the bandwidth coefficient,  $f_c$  is the central frequency of the notch filter and  $f_s$  is the signal sampling rate. The magnitude response of the notch filter is illustrated in Fig. 3. As can be seen from the graphs, the parameter  $\omega$  controls the bandwidth of the notch filter, and the notch filter removes the signal around notch frequencies while keeping the other frequency components close to their original amplitudes. To improve the response and to sharpen the notch in Fig. 3, the signal may be passed through this or a similar digital filter several times to create a cascade. Such a filter designed in MATLAB typically creates around five versions of this.

Suppose that  $f_{a_1}, f_{a_2}$  and  $f_{a_3}$  are the frequencies of the top three ACC spectrum peaks, which are also the central rejection frequencies of the notch filters. In the proposed algorithm, for a central rejection frequency  $f_a, f_a/\mu$  is assumed to be the bandwidth of the notch filter and  $\mu$  is set to 48. The general equation for a notch filter is expressed by

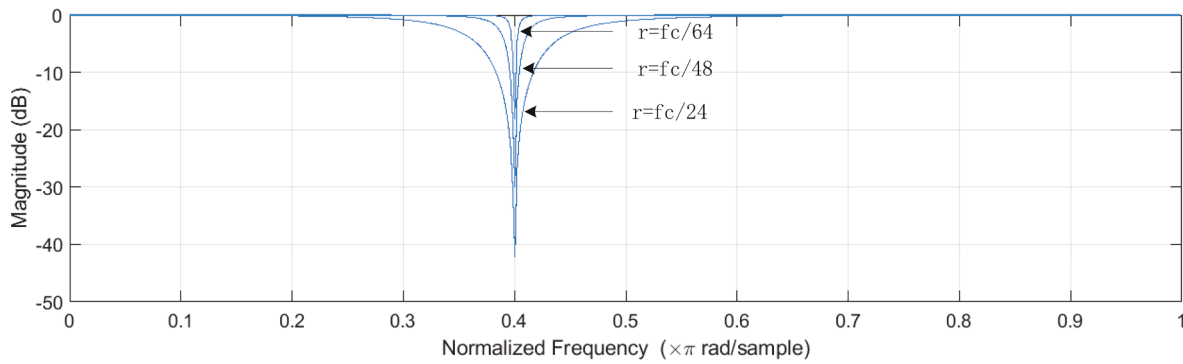


Fig. 3. Magnitude responses of the notch filter.

$$H_{\text{notch}}(f; f_a) = \begin{cases} \delta, & (1 - 1/\mu)f_a \leq f \leq (1 + 1/\mu)f_a \\ 1, & \text{otherwise.} \end{cases} \quad (6)$$

where  $\delta \ll 1$  and  $f_a$  stands for  $f_{a_1}, f_{a_2}$  or  $f_{a_3}$ .

Next, the notch filter, which has adaptive rejection frequencies chosen based on the different scenarios, is applied to the PPG signal recovered in each time window. In the following, different ANF scenarios are discussed to consider cases where the spectral peaks indicating the desired physiological parameters (i.e., HR and RR) are located on the first, second or third PPG spectral peaks, depending upon which PPG peak is closest to the previous calculated physiological parameter value. Here the spectral peak selected to represent the related physiological parameter is labelled  $f_{\text{sel}}$ .

- **Scenario 1:**  $f_{\text{sel}}$  is not found to overlap with any of the three largest ACC spectrum peaks, and so is not affected by the notch filter. Precisely, the peak of the PPG spectrum corresponding to the HR or RR frequency does not coincide with the three leading ACC spectral peaks. In this case, the ANF is comprised of the three notch filters, and is demonstrated in Fig. 4. There, Fig. 4(a2) and (b2) shows the measured PPG signal corrupted with MA. As is apparent, features in the PPG signal in the time-domain (and in the frequency-domain) are poor. It is necessary to remove those frequencies arising from the MA that are related to the ACC reference, these are marked by red circles in Fig. 4(a1) and Fig. 4(a2).
- **Scenario 2:**  $f_{\text{sel}}$  is found to overlap with one of the three largest of the ACC spectral peaks. Fig. 5(a2) shows an example case in which the physiological parameter frequency (indicated by the black circle)

overlaps with the largest of the ACC spectral peak. Continuing with the ANF from *Scenario 1* would filter out the true HR (or RR) frequency, and not recover the desired PPG signals in the time-domain as is illustrated in Fig. 5(a3) and (b3). Clearly the spectral peak should be retained, but the other MA related spectral peak should be removed. The recovered PPG signal in this case is illustrated in Fig. 5 (a4) and (b4). These two scenarios can be combined to express the function of ANF as:

$$H_{\text{ANF}}(f) = \begin{cases} \prod_{k \in \{1,2,3\}} H_{\text{notch}}(f; f_{ak}), & F_{\text{HR/RR}} \not\approx f_{aj} \\ \prod_{k \neq j, k \in \{1,2,3\}} H_{\text{notch}}(f; f_{ak}), & F_{\text{HR/RR}} \approx f_{aj}. \end{cases} \quad (7)$$

### 2.3. Extraction for Physiological Parameters

#### 2.3.1. Heart Rate

Usually, the identified MA are removed and the cleaned PPG signals are recovered effectively in the previous steps. However, in some cases, the sensor may barely capture the PPG signal; for example, if the sensor contact is loose. Thus, a spectral peak calibration and selection are crucial for accurate HR/RR extraction. Prior to these two steps, the HR is calculated as  $HR_{\text{BPM}} = f_{\text{sel}} \times 60$  beats/min, and similarly RR.

- (1) **Calibration:** Calibration mainly ensures that the filtered PPG signals are not still adversely affected by motion. Typically the

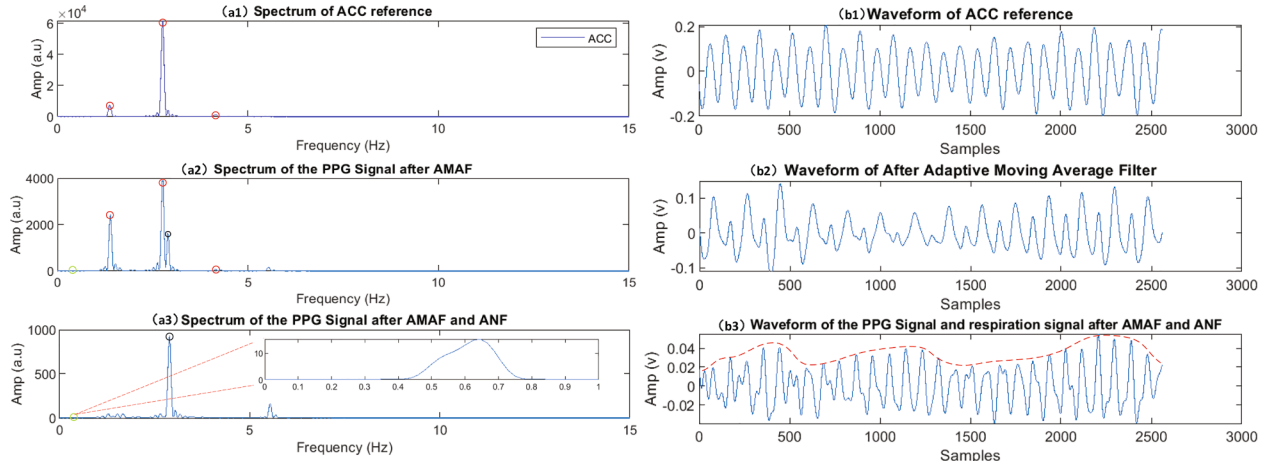
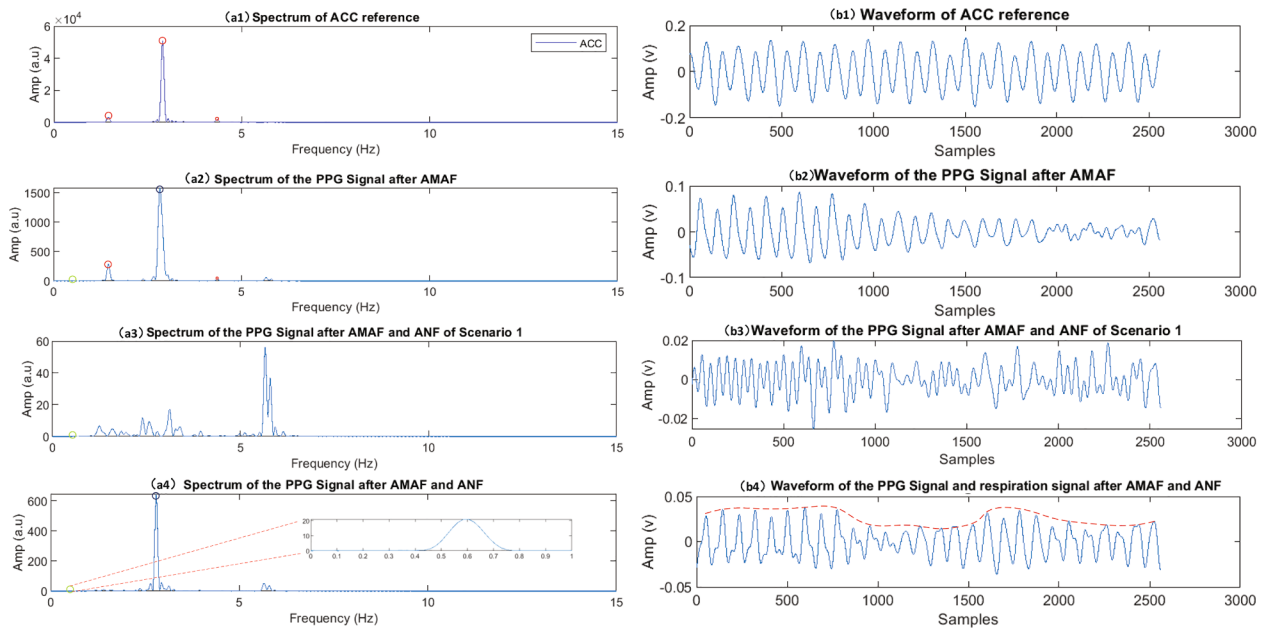


Fig. 4. Detailed processing for the PPG signal when frequencies of the MA are in-band of the PPG signal in Scenario 1. (a1) ACC spectrum peaks as the reference for MA. (b1) ACC signals in time-domain. (a2) corrupted PPG signals with the MA, and the red circle marks coincide with the three most significant spectrum peaks of ACC, and the black and green circles correspond to the frequency of HR and RR. (b2) filtered PPG signals after AMAF in time-domain. (a3) desired PPG signals and respiration signals spectrums. (b3) recovered PPG signals and respiration signals after AMAF and ANF.



**Fig. 5.** Detailed processing for the PPG signal when frequencies of the MA are in-band of the PPG signal in Scenario 2. (a1) ACC spectrum peaks as the reference for MA. (b1) ACC signals in time-domain. (a2) corrupted PPG signals with the MA, and red and black circle marks overlap with the three largest ACC spectrum peaks, but the black and green circles correspond to the frequency of HR and RR. (a3) applying the ANF bandwidth of scenario 1. (b3) its corresponding time-domain waveform. (a4) desired PPG signals and respiration signals spectrums. (b4) its corresponding time-domain waveform.

change in the HR, between successive sliding time window observations, is expected to be limited. Accordingly the following check is performed.

$$|HR_{BPM}[i] - HR_{BPM}[i-1]| < \phi, \quad (8)$$

where  $\phi$  is a tolerance parameter, ensuring that the difference between the current time window heart rate and previous value is within a reasonable tolerance ( $\phi = 10\text{beats/min}$ ). When the rule is satisfied, the current  $HR_{BPM}$  is selected as the final calculated HR. Otherwise, the algorithm moves on to the next part.

(2) **Selection:** The selection deals with the situations of the verification rule (Eq. 8) not being satisfied. For instance, when no satisfactory  $f_{sel}$  is found, the previous HR can be used as a reference, and the PPG spectral peak closest to the reference HR frequency is found denoted as  $f_{sel}'$ . Again,  $f_{sel}'$  is validated by ensuring the difference between  $f_{sel}'$  and previous HR is in a reasonable tolerance (i.e., 10). When  $f_{sel}'$  meets the above requirements, the existing HR is set as  $f_{sel}'$ . Otherwise,  $HR_{BPM}[i]$  is calculated by the trend of the previous three HR values. Specifically, when the trend is upwards (i.e.  $HR[i-3] \leq HR[i-2] \leq HR[i-1]$ ),  $HR_{BPM}[i]$  is set to  $HR_{BPM}[i-1] + 2$ . Again, when the trend is down,  $HR_{BPM}[i]$  is set to  $HR_{BPM}[i-1] - 2$ . Otherwise, the  $HR_{BPM}[i]$  is kept the same as previous HR, i.e.,  $HR_{BPM}[i-1]$ . Finally, the output HR is the average value of the five previous HR values.

### 2.3.2. Respiration Rate

After removing the MA from the PPG signals, the acceleration-derived method is used to extract RR [26]. Precisely, a motion intensity (MI) index is defined using the amplitudes of the 3-axis acceleration signal in the frequency domain (ACC) ( $Amp_{ACC}$ ).

$$MI = \begin{cases} \text{low} & Amp_{ACC} \leq 100, \\ \text{medium} & 100 < Amp_{ACC} \leq 400, \\ \text{high} & Amp_{ACC} > 400. \end{cases} \quad (9)$$

Again, the cut-off parameters of 8<sup>th</sup> order IIR Butterworth bandpass filter are selected adaptively. When the MI is low, the passband of the band-pass filter is set to 0.2–0.5 Hz; when MI is medium, the passband is

set to 0.3–0.7 Hz and when MI is high the passband is set to 0.4–0.9 Hz. Thereafter, the RR can be obtained from the peak in the frequency domain FFT. As with  $th_1$  used previously, the thresholds defining MI will need to be scaled by a factor of  $N_{FFT}/8192$  for shorter block FFTs.

### 2.4. Parameter Settings

For the LU-Db dataset the sampling rate ( $F_s$ ) is 256 Hz, the time window sliding along the signals is 10 s long with HR values (using the ANFA) extracted in 1 s intervals, and the number of FFT points ( $N_{FFT}$ ) is set at 8192. In general we recommended that  $N_{FFT}$  is set so that each frequency bin ( $F_s/N_{FFT} \times 60$ ) corresponds to about 1 beats/min. By contrast for the IEEE-SPC dataset, the sampling rate is  $F_s = 128\text{Hz}$  so  $N_{FFT}$  is set at 4096. Here, the time window is 8 s long with an incremental step of 2 s.

### 2.5. Measurement Protocol

The ANFA was conducted with two databases: a) Loughborough University database (LU-Db) and b) IEEE Signal Processing Cup (SPC) 2015. LU-Db was well suited for the validation using two forms of exercise with four different physical activity intensities, e.g., 1) cycling, and 2) running. The SPC database was used as a benchmark for verification of state-of-the-art signal processing algorithms. Specifically, with LU-Db, 12 healthy subjects (aged  $24 \pm 3$  years, two females and ten males) undertook the protocol which was approved by the Loughborough University Ethical Advisory Committee.

During the protocol implementation, a reference HR was recorded using a Polar Bluetooth® Smart chest strap (Polar, Electro, Kempele, Finland) [27]. RR was also determined using a Vynntus™ CPX Metabolic cart (JAEGER™ Vynntus™ CPX, Carefusion, Germany). The mOEPS sensor with 3-axis acceleration as a MA reference was placed on the subject's thumb. During data recording, the subjects performed the following exercise: 1) cycling at four different levels of resistance 2) walking, and 3) running on a treadmill at different speeds. In these designated exercises, the female subjects cycled at 60, 90, 120 and 150 watts and the male subjects cycled at 90, 120, 150 and 180 watts, and all subjects walked or ran on a treadmill at 3, 6, 9 and 12 km/h for 4 min at

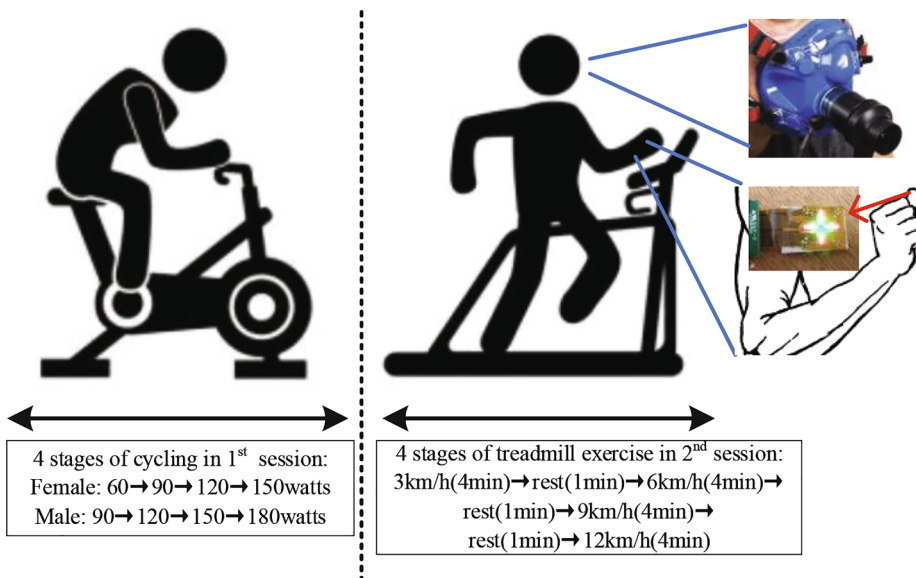


**Fig. 6.** Illustration of the exercise protocol during multi-stage cycle (1<sup>st</sup> session) and treadmill (2<sup>nd</sup> session) tests. The location of mOEPS sensor and respiration rate measurement sensor.

each intensity with 1 min rest before the exercise intensity was increased. Fig. 6 displays several subjects with the actual testing environment and equipment.

The IEEE-SPC database comprises of PPG signals of 5-min duration from 12 healthy subjects aged 18 to 35 [20]. The dataset for each subject comprises one channel of PPG signals obtained from the mOEPS corresponding with green LEDs (illumination wavelength: 525 nm), the 3-axis acceleration signals from the wrist, and the ECG signal from the chest using wet ECG sensors. During data recording, the subjects walked or ran on a treadmill with the following speeds in order: 6 km/h for a period of 60 s; 12 km/h for a period of 60 s; 6 km/h for a period of 60 s; 12 km/h for a period of 60 s each stage was followed by a 30 s break.

### 3. Results of Physiological Monitoring

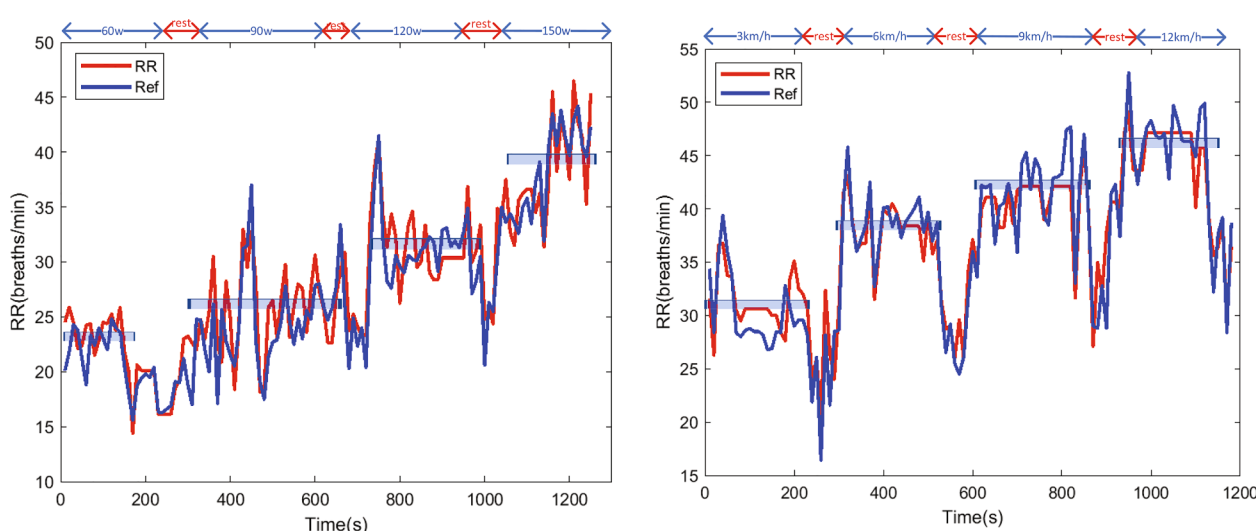
#### 3.1. Physiological parameters from signal processing

The results of continuous HR and RR monitoring for two different subjects in LU-Db dataset are presented by the ANFA in Fig. 7(a), Fig. 7(b), Fig. 7(b), and Fig. 8(b). The ground-truth HR generated by the chest

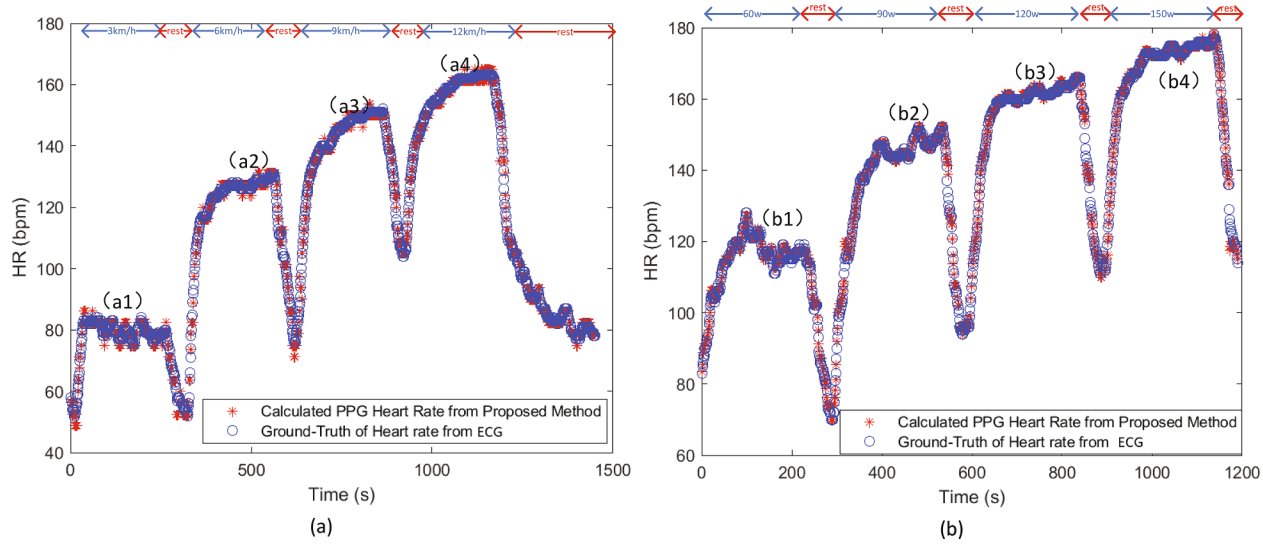
strap and the reference RR measured by the metabolic cart are also shown in Figs. 7 and 8. It is observed that, for the ANFA, the RR and HR performance is very robust, and highly accurate in tracking the reference RR at different exercise intensities, and it can be observed that the average RR increases as the physical activity intensity increases.

Fig. 9 and Fig. 10 show the detailed PPG signals in the time-domain correspond to the different physical activity intensity points as shown in Fig. 8(a) and (b). (a1) is selected at an intensity of 3 km/h. Again, (a2), (a3) and (a4) are selected at intensities of 6 km/h, 9 km/h and 12 km/h respectively. (b1), (b2), (b3) and (b4) are chosen in the same way.

Table 1 expresses the average absolute error ( $\epsilon_1$ ) and the average error percentage ( $\epsilon_2$ ) for 12 subjects from the LU-Db datasets, 1<sup>st</sup> and 2<sup>nd</sup> sessions are listed, respectively. Satisfactory results are attained by using the ANFA. In the 1<sup>st</sup> session, through an average of all 12 subjects' recordings, the average  $\epsilon_1 = 1.07 \pm 0.17$  beats/min (mean  $\pm$  std), and the average  $\epsilon_2 = 1.04\%$ . Furthermore, in the 2<sup>nd</sup> session, the average  $\epsilon_1$  is  $1.50 \pm 0.28$  beats/min (mean  $\pm$  std), and the average  $\epsilon_2$  is 1.26%. The



**Fig. 7.** RR calculation results on two subjects chosen LU-Db datasets. (a) The results of subject F03 in 1<sup>st</sup> session. (b) The results of subject M08 in 2<sup>nd</sup> session.



**Fig. 8.** HR calculation results on two subjects chosen LU-Db datasets. (a) The results of subject F03 in 1<sup>st</sup> session. (b) The results of subject M08 in 2<sup>nd</sup> session.

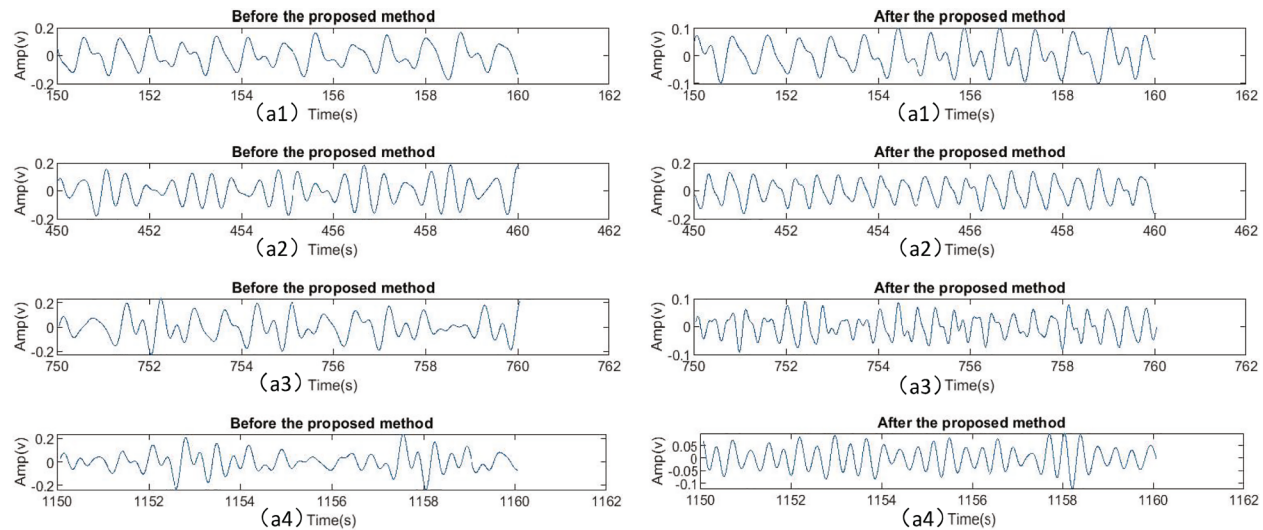


**Fig. 9.** Detailed PPG signals in the time domain correspond to different points in Fig. 8(a).

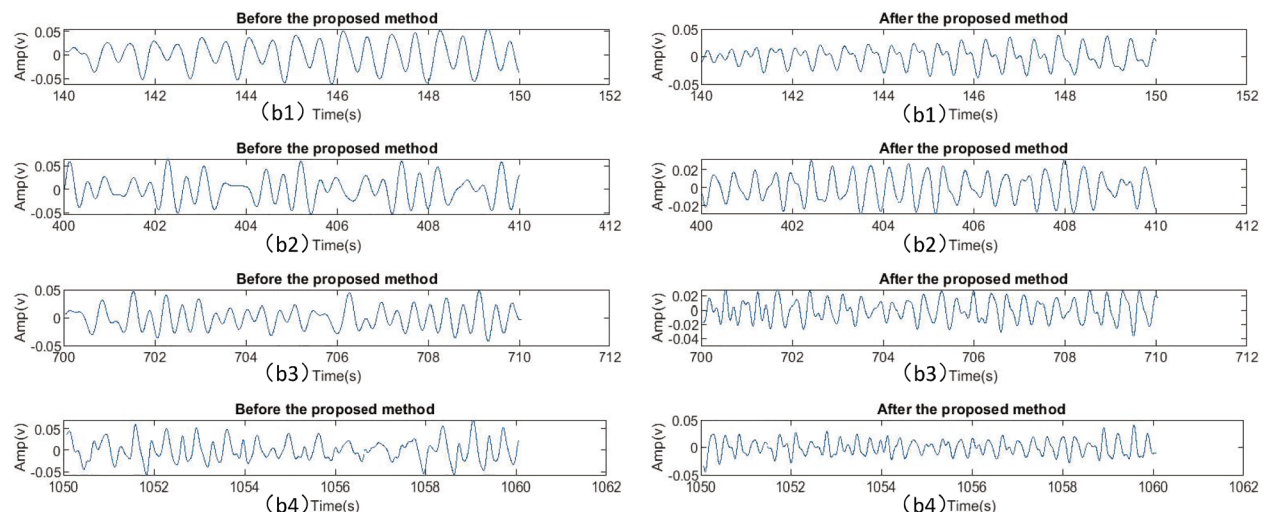


**Fig. 10.** Detailed PPG signals in the time domain correspond to different points in Fig. 8(b).

**Table 1**

Average Absolute Error ( $\epsilon_1$ ) (in beats/min) and Average Absolute Error Percentage ( $\epsilon_2(\%)$ ) on all 12 subjects (F-female, M-male) of LU-Db with different sessions.

Subj	F01	F02	F03	M04	M05	M06	M07	M08	M09	M10	M11	M12
1 <sup>st</sup>	$\epsilon_1$	0.91	1.16	1.15	0.93	1.01	1.25	1.04	0.73	1.21	1.32	1.22
	$\epsilon_2$	0.72	1.10	0.99	0.97	0.79	1.18	1.07	0.91	1.12	1.37	1.40
2 <sup>nd</sup>	$\epsilon_1$	1.52	1.47	1.16	1.35	1.31	1.37	1.37	1.49	1.27	2.19	1.67
	$\epsilon_2$	1.08	1.03	0.90	1.02	1.10	1.05	1.18	1.48	1.02	2.11	1.58

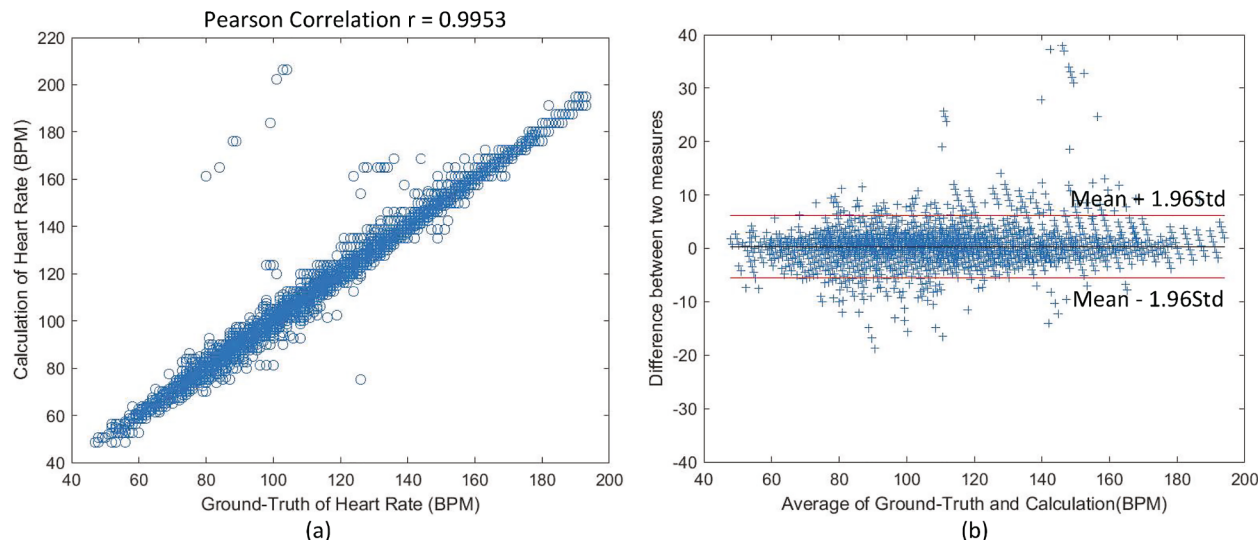


**Fig. 11.** HR calculation results on 12 subjects of LU-Db with 1<sup>st</sup> and 2<sup>nd</sup> sessions (BPM: beats/min). (a) Pearson correlation plot. (b) Bland–Altman plot against ground-truth and calculated HR.

**Table 2**

Average Absolute Error ( $\epsilon_1$ ) (in breaths/min) on all 12 subjects (F-female, M-male) of LU-Db datasets with different sessions.

Subj	F01	F02	F03	M04	M05	M06	M07	M08	M09	M10	M11	M12
1 <sup>st</sup>	$\epsilon_1$	3.07	2.16	2.25	2.81	2.41	3.16	2.24	2.17	2.65	2.79	2.47
	$\epsilon_2$	2.94	2.95	2.72	2.81	3.17	3.23	3.17	3.09	2.96	3.01	2.86
2 <sup>nd</sup>	$\epsilon_1$											3.02

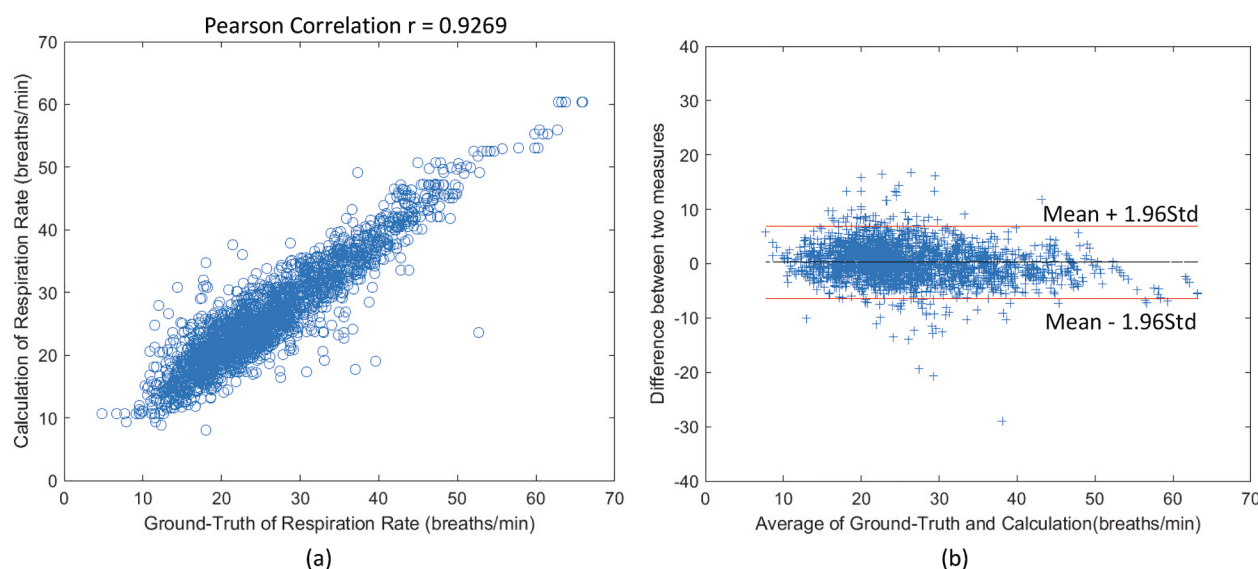


**Fig. 12.** RR calculation results on 12 subject datasets of LU-Db with 1<sup>st</sup> and 2<sup>nd</sup> sessions. (a) Pearson correlation plot. (b) Bland–Altman plot against ground-truth and calculated RR.

Bland–Altman plot between the ground-truth HR (ECG) and the calculated HR (PPG) is shown in Fig. 11(b). The Limit of Agreement (LOA) is [-5.54, 6.19] beats/min with standard deviation  $\sigma = 2.99$  in the two sessions, and 95% of all differences are inside this range. Fig. 11(a) illustrates the scatter plot between the ground-truth HR and the related estimates on 12 subjects in LU-Db with the Pearson Correlation  $r : 0.9953$ .

Table 2 illustrates the  $\epsilon_1$  values of RR in the 1<sup>st</sup> and 2<sup>nd</sup> sessions for 12 subjects, and average  $\epsilon_1$  in different sessions are  $2.56 \pm 0.34$  (mean  $\pm$  std) and  $2.99 \pm 0.15$  (mean  $\pm$  std) breaths/min, respectively. Fig. 12(a) displays the scatter plot between the ground-truth and calculated RR on 12 subjects in LU-Db with the Pearson Correlation  $r : 0.9269$ . Additionally, the Bland–Altman plot is applied for all 12 subjects, is given in Fig. 12(b). The LOA between the ground-truth and the calculated RR data is [-6.41, 6.87] breath/min.

### 3.2. Comparative results

To better represent the performance of the ANFA, the IEEE-SPC dataset is adopted as a benchmark for comparison of the proposed algorithm with other recently reported algorithms as shown in Table 3. It is observed that the ANFA performance exceeds that of the other algorithms in terms of overall mean error ( $\epsilon_1$ ). Table 4 shows that the ANFA has fewer tunable parameters compared to other algorithms listed. Fewer user-tunable parameters could simplify the complexity of the algorithm and improve the generalization performance on other datasets.

### 3.3. Down-sampling Processing

To perform the ANFA in a near-real-time situation, the memory size and the required number of clock cycles of the embedded system are considered to be crucial indicators to testify the algorithm performance. The computational complexity here depends largely upon the FFT operation and the filtering, in the ANFA. Referring to the actual embedded memory and clock cycle, taking ARM Cortex-3 as an example, it supports a maximum of 1024-point FFT operations and the required time is 187204 clock cycles [30]. The ANFA using 8192-point FFT may not meet the computing and memory requirements of embedded systems. Thus, ANFA with 1024-point FFT could be applied to achieve the near-real-time signal processing through the down-sampling processing, which means that a 64 Hz of sampling rate could be taken to perform the 1024-point FFT operation rather than 256 Hz sampling rate. The comparative results of ANFA with 1024-point FFT and 8192-point FFT are presented in Fig. 13. Additionally, Table 5 illustrates the comparative results between ANFA with 1024-point FFT and 8192-point FFT of the HR average absolute error on all 12 subjects of LU-Db datasets, and it also presents that the ANFA is not significantly affect the measurement

accuracy of the physiological parameters during the down-sampling processing.

## 4. Discussion

Although the acceleration-based adaptive filter could improve the accuracy of HR calculation, such adaptive filters are still dependent on the signal quality of the reference acceleration signal [28]. Previous work by Nabavi and colleagues [19] addressed this issue by proposing the bandstop filter based on the 3-axis acceleration reference, the work was mainly proposed to address the motion scenarios during lower intensity. The ANFA described in the present study has effectively removed MA and recovered cleansed PPG signals using a reference signal from the 3-axis accelerometer at different motion intensities. In spite of the application of bandstop or notch filters, in noise-free PPG signal extraction, having been used before [1] [24], the calculation accuracy still needs to be improved. In this study, the proposed solution creates a algorithm to accurately extract HR and RR, and provides a flexible combination of notch filters to retain physiological information in these PPG signal datasets, making it easier to extract accurate physiological parameters. At this point, the ANFA could represent an improved solution for embedded, real-time, wearable detection devices due to its low complexity.

Comparing with other algorithms, the ANFA has an improved HR/RR calculation performance. Specifically, the adaptability of the ANFA gives it an advantage in removing MA in different motion intensities, much superior to fixed bandstop filters [1]. Table 3 presents the better performance of ANFA for the IEEE-SPC dataset. Although the average error result of the ANFA is only marginally better (0.01 beats/min) than method in [24], the error between datasets (std) is lower than in [24]. Additionally, the ANFA shows it is capable of extracting accurate HR at four stages of increasing intensity on a cycle ergometer and a treadmill compared to standard commercial devices.

Conversely, the accuracy of RR extraction has a larger  $\epsilon_1$  compared to the HR measurement, which is  $2.56 \pm 0.34$  and  $2.99 \pm 0.15$  breaths/min in cycling and treadmill exercise with different physical activity intensities. On the other hand, the RR is located in a much lower frequency range (0.1–1.0 Hz), and it is more susceptible to interference from MA than HR measurement [31]. As shown in Fig. 7, the measured RR was broadly consistent with the reference RR trend, and it also shows the same step-wise increase with increasing exercise intensity. Again, to make the ANFA applicable, a low-complexity and efficient method is adopted for RR extraction, but it is possible that it may reduce the extraction accuracy.

Furthermore, the methods as reported in Table 4 follow a number of heuristic rules and thresholds. For instance, the MA removal as presented in [20,24,16,6,28,29] requires several parameters to be defined. Increasing the number of tunable parameters of designated algorithms

**Table 3**

Average Absolute Error ( $\epsilon_1$ ) (in beats/min) on the IEEE-SPC of the ANFA along with the same of other recently reported results.

Subject	TROIKA [20]	Wang [24]	MUARD [16]	Zhao. [6]	Arunkumar et al. [28]	Zhang. [29]	ANFA
1	2.29	1.09	1.17	1.23	1.13	2.06	1.08
2	2.19	0.87	0.93	1.51	0.87	3.59	0.94
3	2.00	1.20	0.70	1.19	0.73	0.92	0.74
4	2.15	0.81	0.82	0.92	0.95	1.54	0.75
5	2.01	0.67	0.88	0.61	0.85	0.97	0.69
6	2.76	1.15	0.97	0.78	0.94	1.64	0.89
7	1.67	0.73	0.67	0.48	0.66	2.25	0.73
8	1.93	0.49	0.74	0.56	0.70	0.63	0.60
9	1.86	0.34	0.49	0.49	0.59	0.62	0.61
10	4.70	2.06	2.69	3.81	3.94	4.62	1.94
11	1.72	0.87	0.81	0.78	1.01	1.30	0.92
12	2.84	0.78	0.77	1.04	0.95	1.80	0.99
Mean	2.32	0.92	0.97	1.06	1.11	1.83	0.91
(Std)	(0.84)	(0.44)	(0.57)	(0.91)	(0.90)	(1.21)	(0.36)

**Table 4**

The number of user-tunable parameters in MA-removal and HR tracking and validation steps.

Tunable threshold	TROIKA [20]	Wang [24]	MUARD [16]	Zhao. [6]	Arunkumar et al. [28]	Zhang. [29]	ANFA
MA-Removal	>10	5	6	>10	>10	6	4
HR tracking and validation	>10	4	2	2	3	2	2

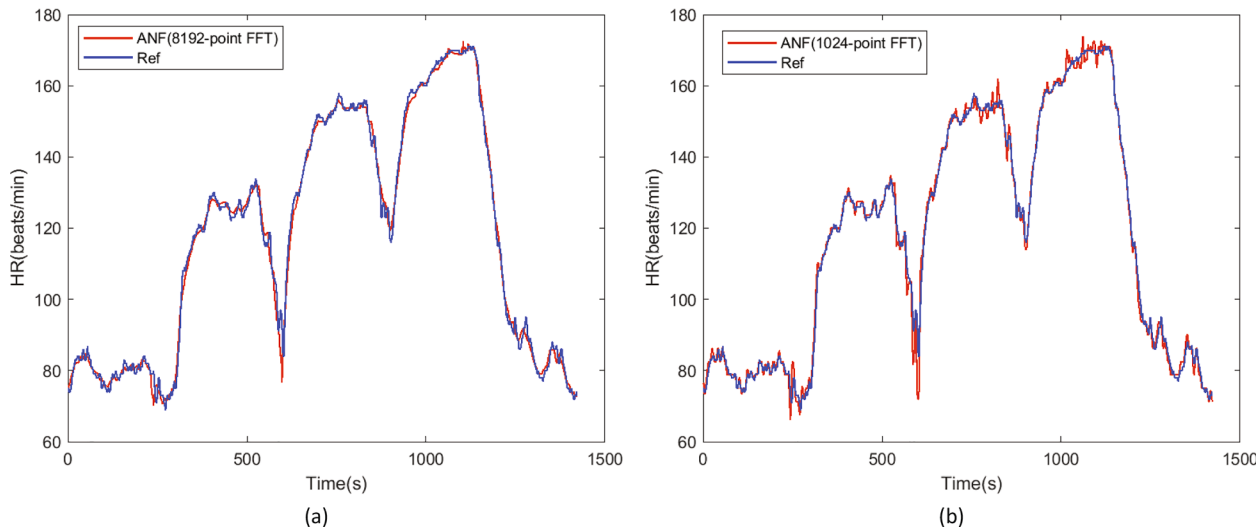


**Fig. 13.** The comparison result of ANFA with 1024-point FFT and 8192-point FFT on M011 subject chosen LU-Db datasets. (a) ANFA with 8192-point FFT. (b) ANFA with 1024-point FFT.

**Table 5**

Average Absolute Error ( $\epsilon_1$ ) (in beats/min) on all 12 subjects (F-female, M-male) of LU-Db with different FFT-point, i.e., 8192 and 1024-point.

	FFT-point	F01	F02	F03	M04	M05	M06	M07	M08	M09	M10	M11	M12
1 <sup>st</sup>	8192	0.91	1.16	1.15	0.93	1.01	1.25	1.04	0.73	1.21	1.32	1.22	0.93
	1024	1.03	1.29	1.43	1.07	1.49	1.58	1.47	1.61	1.52	1.47	1.43	1.09
2 <sup>nd</sup>	8192	1.52	1.47	1.16	1.35	1.31	1.37	1.37	1.49	1.27	2.19	1.67	1.78
	1024	1.73	1.63	1.26	1.52	1.61	1.86	1.57	1.83	1.62	2.67	1.98	2.09

could lead to an improved performance but it is also likely to increase complexity of the signal processing and lead to a risk of poor generalisation on physiological monitoring datasets with MA. Although the present ANFA runs on a PC, its performance has demonstrated that the ANFA could be easily deployed onto a wearable embedded platform with the mOEPS.

To perform the ANFA in a near-real-time situation, the memory size of the embedded system has been considered as a crucial indicator to testify the algorithm performance. The computational complexity depends largely upon the FFT operation and the filter implementation in the ANFA. Specifically, the ANFA adopted four  $N_{FFT}$ -point FFTs with a zero padding operation, i.e., ACC spectrum, PPG spectrum, HR calculation and RR calculation, and  $N_{FFT}$ -point was set as 8192. The ANFA, with 1024-point FFT, has been considered as the simplest way of achieving the near-real-time signal processing through the down-sampling which is routinely possible using the most readily available ARM based 32-bit MCUs, as shown in Fig. 13 and Table 5. To meet the actual embedded timing requirements, a 64 Hz sampling rate (down-sampled from 256 Hz) allows 1024-point FFT operation. Four 1024-point FFTs requires  $4 * 187204 \approx 0.75M$  clock cycles, and a ARM Cortex 3 MCU running at 100 MHz would mean that FFT calculation is not too much of a concern in the present study [30]. Two of the filters used are fixed so that tap coefficients can easily be stored on chip. The final (notch) filter needs to be adaptive (tap coefficients depend on the value of  $f_a$ ). Dependent on the hardware used, and the memory allocation allowed, a look up table with hardware appropriate granularity and

an interpolation scheme can be used. The notch filters used here were made from five cascaded 2<sup>nd</sup> order IIR filters, so that each complete filter requires 25 tap coefficients. With  $f_a$  values from (say) 31 Hz to 230 Hz at a granularity of 1 Hz would need  $25 \times 200 = 5000$  Floating Point numbers or 20 kB of memory, a small fraction of available space.

## 5. Conclusion

The study has demonstrated that the ANFA can better remove MA than those available methods as stated in the section of Results, allowing for the extraction of two key physiological parameters, i.e., HR and RR, for health monitoring during physical activity/exercise.

The ANFA, as described in the section of Methodology and Materials, demonstrates the removal of MA using a low complexity and intuitive method, thus making real-time signal processing achievable. With the ANFA, the AMAF Box plays a critical role in removing out-of-band noise, and the ANFA works on the removal of in-band noise by the means of 3-axis acceleration reference. HR and RR, being critical physiological parameters, are obtained with a sliding time window, thus recovering the distinctive PPG signals.

The ANFA has been well applied to the LB-Db and IEEE-SPC datasets to generate accurate HR and RR readings compared to those available methods. The outcome from the study has illustrated that the ANFA could effectively recover the desired PPG signals, in real-time, even when the subject is exercising at different intensities.

## Author Contributions

XZ carried out the study, the signal processing, and wrote the manuscript. VMD provided background knowledge and advised on original work, co-supervised the study. LAB provided exercise protocol and advised on original work, co-supervised the study. MD jointly supervised the study and reviewed the manuscript. SH structured the manuscript, analyzed the outcomes, and supervised the study.

## Declaration of Competing Interest

The authors declare that they have no known competing financial interests or personal relationships that could have appeared to influence the work reported in this paper.

## Acknowledgments

The authors would like to acknowledge the support of Loughborough University in the conduction of this study, and the shared the datasets from the IEEE-SPC.

## References

- [1] S. Nabavi, S. Bhadra, A robust fusion method for motion artifacts reduction in photoplethysmography signal, *IEEE Trans. Instrum. Meas.* 69 (12) (2020) 9599–9608, <https://doi.org/10.1109/TIM.2020.3006636>.
- [2] M. Schmidt, A. Schumann, J. Miller, K.-J. Bar, G. Rose, ECG derived respiration: Comparison of time-domain approaches and application to altered breathing patterns of patients with schizophrenia, *Physiol. Meas.* 38 (2017) 601, <https://doi.org/10.1088/1361-6579/aa5feb>.
- [3] W. Lin, D. Wu, C. Li, H. Zhang, Y. Zhang, Comparison of heart rate variability from PPG with that from ECG, *Int. Conf. Health Inform.* 42 (2017) 213–215, [https://doi.org/10.1007/978-3-319-30005-0\\_54](https://doi.org/10.1007/978-3-319-30005-0_54).
- [4] D. Biswas, N. Simões-Capela, C. Van Hoof, N. Van Helleputte, Heart rate estimation from wrist-worn photoplethysmography: A review, *IEEE Sensors J.* 19 (2019) 6560–6570, <https://doi.org/10.1109/JSEN.2019.2914166>.
- [5] H. Chung, H. Lee, J. Lee, Finite state machine framework for instantaneous heart rate validation using wearable photoplethysmography during intensive exercise, *IEEE J. Biomed. Health Inform.* 23 (4) 1595–1606, doi: 10.1109/JBHI.2018.2871177.
- [6] D. Zhao, Y. Sun, S. Wan, F. Wang, Sfst: A robust framework for heart rate monitoring from photoplethysmography signals during physical activities, *Biomed. Signal Process. Control* 33 (2017) 316–324, <https://doi.org/10.1016/j.bspc.2016.12.005>.
- [7] N.K.L. Murthy, P.C. Madhusudana, P. Suresha, V. Periyasamy, P.K. Ghosh, Multiple spectral peak tracking for heart rate monitoring from photoplethysmography signal during intensive physical exercise, *IEEE Signal Process. Lett.* 22 (12) (2015) 2391–2395, <https://doi.org/10.1109/LSP.2015.2486681>.
- [8] B.S. Kim, S.K. Yoo, Motion artifact reduction in photoplethysmography using independent component analysis, *IEEE Trans. Biomed. Eng.* 53 (3) (2006) 566–568, <https://doi.org/10.1109/TBME.2005.869784>.
- [9] R. Krishnan, B. Natarajan, S. Warren, Two-stage approach for detection and reduction of motion artifacts in photoplethysmographic data, *IEEE Trans. Biomed. Eng.* 57 (8) (2010) 1867–1876, <https://doi.org/10.1109/TBME.2009.2039568>.
- [10] E. Khan, F. Al Hossain, S.Z. Uddin, S.K. Alam, M.K. Hasan, A robust heart rate monitoring scheme using photoplethysmographic signals corrupted by intense motion artifacts, *IEEE Trans. Biomed. Eng.* 63 (3) (2015) 550–562, doi: 10.1109/TBME.2015.2466075.
- [11] M.A. Motin, C.K. Karmakar, M. Palaniswami, Selection of empirical mode decomposition techniques for extracting breathing rate from ppg, *IEEE Signal Process. Lett.* 26 (4) (2019) 592–596, <https://doi.org/10.1109/LSP.2019.2900923>.
- [12] M. Raghuvaran, K.V. Madhav, E.H. Krishna, K.A. Reddy, Evaluation of wavelets for reduction of motion artifacts in photoplethysmographic signals, in: 10th Int. Conf. Inf. Sci., Signal Process. Their Appl. (ISSPA 2010), 2010, pp. 460–463, doi: 10.1109/ISSPA.2010.5605443.
- [13] A. Galli, C. Narduzzi, G. Giorgi, Measuring heart rate during physical exercise by subspace decomposition and kalman smoothing, *IEEE Trans. Instrum. Meas.* 67 (5) (2017) 1102–1110, <https://doi.org/10.1109/TIM.2017.2770818>.
- [14] A. Koneshloo, D. Du, A novel motion artifact removal method via joint basis pursuit linear program to accurately monitor heart rate, *IEEE Sensors J.* 19 (21) (2019) 9945–9952, <https://doi.org/10.1109/JSEN.2019.2927994>.
- [15] H. Fukushima, H. Kawanaka, M.S. Bhuiyan, K. Oguri, Estimating heart rate using wrist-type photoplethysmography and acceleration sensor while running, in, Int'l Conf IEEE Eng Med Bio Soc (EMBC) (2012) 2901–2904, <https://doi.org/10.1109/EMBC.2012.6346570>.
- [16] S.S. Chowdhury, R. Hyder, M.S.B. Hafiz, M.A. Haque, Real-time robust heart rate estimation from wrist-type ppg signals using multiple reference adaptive noise cancellation, *IEEE J. Biomed. Health Inform.* 22 (2) (2016) 450–459, <https://doi.org/10.1109/JBHI.2016.2632201>.
- [17] M.R. Ram, K.V. Madhav, E.H. Krishna, N.R. Komalla, K.A. Reddy, A novel approach for motion artifact reduction in ppg signals based on as-lms adaptive filter, *IEEE Trans. Instrum. Meas.* 61 (5) (2011) 1445–1457, <https://doi.org/10.1109/TIM.2011.2175832>.
- [18] R. Yousefi, M. Nourani, S. Ostadabbas, I. Panahi, A motion-tolerant adaptive algorithm for wearable photoplethysmographic biosensors, *IEEE J. Biomed. Health Inform.* 18 (2) (2013) 670–681, <https://doi.org/10.1109/JBHI.2013.2264358>.
- [19] S. Nabavi, S. Debbarma, S. Bhadra, Measurement of cardiac parameters by motion artifacts free photoplethysmography signals, in: Conf IEEE Int. Instrum. Meas. Technol. (I2MTC), 2020, pp. 1–6, doi: 10.1109/I2MTC43012.2020.9128713.
- [20] Z. Zhang, Z. Pi, B. Liu, Troika: A general framework for heart rate monitoring using wrist-type photoplethysmographic signals during intensive physical exercise, *IEEE Trans. Biomed. Eng.* 62 (2) (2014) 522–531, <https://doi.org/10.1109/TBME.2014.2359372>.
- [21] Z. Zhang, Photoplethysmography-based heart rate monitoring in physical activities via joint sparse spectrum reconstruction, *IEEE Trans. Biomed. Eng.* 62 (8) (2015) 1902–1910, <https://doi.org/10.1109/TBME.2015.2406332>.
- [22] S. Salehizadeh, D. Dao, J. Bolkhovsky, C. Cho, Y. Mendelson, K.H. Chon, A novel time-varying spectral filtering algorithm for reconstruction of motion artifact corrupted heart rate signals during intense physical activities using a wearable photoplethysmogram sensor, *Sensors (MDPI)* 16 (1) (2016) 10, <https://doi.org/10.3390/s16010010>.
- [23] M.T. Islam, S.T. Ahmed, C. Shahnaz, S.A. Fattah, Specmar: Fast heart rate estimation from ppg signal using a modified spectral subtraction scheme with composite motion artifacts reference generation, *Med. Biol. Eng. Comput.* 57 (3) (2019) 689–702, <https://doi.org/10.1007/s11517-018-1909-x>.
- [24] M. Wang, Z. Li, Q. Zhang, G. Wang, Removal of motion artifacts in photoplethysmograph sensors during intensive exercise for accurate heart rate calculation based on frequency estimation and notch filtering, *Sensors (MDPI)* 19 (15) (2019) 3312, <https://doi.org/10.3390/s19153312>.
- [25] C.-C. Tseng, S.-C. Pei, Stable iir notch filter design with optimal pole placement, *IEEE Trans. Signal Process.* 49 (11) (2001) 2673–2681, <https://doi.org/10.1109/78.960414>.
- [26] G.-Z. Liu, Y.-W. Guo, Q.-S. Zhu, B.-Y. Huang, L. Wang, Estimation of respiration rate from three-dimensional acceleration data based on body sensor network, *Telemed. E-health* 17 (9) (2011) 705–711, <https://doi.org/10.1089/tmj.2011.0022>.
- [27] A. Alzahrani, S. Hu, V. Azorin-Peris, L. Barrett, D. Esliger, M. Hayes, S. Akbare, J. Achart, S. Kuoch, A multi-channel opto-electronic sensor to accurately monitor heart rate against motion artefact during exercise, *Sensors (MDPI)* 15 (10) (2015) 25681–25702, <https://doi.org/10.3390/s151025681>.
- [28] K. Arunkumar, M. Bhaskar, Heart rate estimation from wrist-type photoplethysmography signals during physical exercise, *Biom. Signal Process. Control* 57 (2020), 101790, <https://doi.org/10.1016/j.bspc.2019.101790>.
- [29] Y. Zhang, B. Liu, Z. Zhang, Combining ensemble empirical mode decomposition with spectrum subtraction technique for heart rate monitoring using wrist-type photoplethysmography, *Biomed. Signal Process. Control* 21 (2015) 119–125, <https://doi.org/10.1016/j.bspc.2015.05.006>.
- [30] T. Lorenser, The dsp capabilities of arm cortex-m4 and cortex-m7 processors, *ARM White Paper* 29 (2016).
- [31] P. Kuwalek, B. Burlaga, W. Jesko, P. Konieczka, Research on methods for detecting respiratory rate from photoplethysmographic signal, *Biomed. Signal Process. Control* 66 (2021), 102483, <https://doi.org/10.1016/j.bspc.2021.102483>.